This manuscript in post-review format was accepted for publication in Journal of Composite Materials, and can be cited as follows

G. Pierreux, D. Van Hemelrijck, T.J. Massart, Automated RVE computations for evaluation of microdamage initiation in structural stitched non-crimp fabric composites, Journal of Composite Materials, In Press.

Automated RVE computations for evaluation of microdamage initiation in structural stitched non-crimp fabric composites

Gerrit Pierreux[a,b,*], Danny Van Hemelrijck[a], Thierry J.Massart[b]

[a] *Vrije Universiteit Brussel, Department of Mechanics of Materials and Constructions, Pleinlaan 2, 1050 Brussels, Belgium*
[b] *Universite Libre de Bruxelles, Building, Architecture and Town Planning Dept., Avenue Fr. Roosevelt 50, CP 194/02, 1050 Brussels, Belgium*

Abstract

This contribution presents an approach to generate unit-cell models of structural stitched non-crimp fabric composites. Resin-rich regions and out-of-plane undulations caused by the stitching yarn are represented by initially straight discretised lines, while the stitching yarn is represented initially by a single discretised line which can be transformed into a multi-line configuration to model stitch cross-section variations. The discretised lines are shaped by geometrical operations with a contact treatment and boundary conditions being used to account, respectively, for line interactions and to control the shape of the bottom and top surfaces of each lamina respectively. A fiber-reinforced distorted zone with local variations in fiber volume fraction and fiber direction is modelled in cross-sections of the lamina in a post-processing step. Models for different stacking sequences and stitching parameters are then automatically generated and subsequently being in the stiffness calculation and damage initiation assessment using finite element based mechanical simulations.

Keywords: structural stitched non-crimp fabric composites, geometrical model generation, mechanical simulation, deformable stitching yarn.

1. Introduction

Stitching is a technique by which a high-strength stitching yarn can be inserted through the thickness of non-crimp fabric laminates to increase their out-of-plane properties [1–3]. The out-of-plane properties can be tailored by stitch parameters such as stitch content, diameter, pattern and

*Corresponding author
E-mail address: gerrit.pierreux@gmail.com (G. Pierreux).

tensioning [4–7]. However, the insertion of the stitching yarn distorts the in-plane fiber-reinforced regions. Experimental investigations have been ambiguous on whether the in-plane mechanical properties are increased, decreased, or remain unchanged by these distortions [3, 8–13]. On the other hand, it is generally accepted that stitching sites are acting as stress concentrations regions which causes early damage initation. [9, 10, 14–18]. Unit-cell models have been shown a valuable approach to help understanding trends from experimental observations as a function of the underlying reinforcement geometry [19, 20]. The main geometrical features of the reinforcement architecture should then be characterised and be included in these models [21, 22].

Resin-rich regions, local fiber-reinforced distorted zones, out-of-plane undulations in the surface lamina and a deformable stitching yarn are the main features present in stitched non-crimp fabrics composites. Their shape and size further depend on the stitching parameters and on the main fiber direction in each lamina, with respect to the stitch direction (Fig. 1a) [21–24]. Eyelet-shaped resin-rich regions arise for small stitch content and can evolve into channel-shaped resin-rich regions for larger stitch content in laminae in which the fibers are aligned in one of the stitch pattern directions (Fig. 1b). The width of the resin-rich regions in a lamina depends on the angle between the main fiber direction in the lamina and the stitch direction (Fig. 1b) and is larger in a surface lamina compared to an inner lamina. Asymmetrically shaped resin-rich regions are present in laminae with fibers not aligned in one of the stitch pattern directions [9]. Local variations in fiber volume fraction and fiber misalignment are present in the fiber-reinforced distortions zone [25]. Centerline deflections and cross-section shape variations of the stitching yarn should be conform with the neighbouring lamina distortions and are further affected by the stitching yarn tensioning, and by transverse compaction processes. Non-crimp fabric composites have further comparable (but smaller) geometrical features [26–30] while stitching imperfections may also results in certain geometrical features of the reinforcement architecture (as fiber-weaving [31–33], an inclined through-the-thickness segment of the stitching yarn [23], crimp of the through-the-thickness segment [21], or fiber breakage due to stitch insertion [11]).

Analytical modelling approaches have been adopted in literature to include the presented features in geometrical unit-cell models in which the laminae were often assumed straight [10, 23, 34–37]. The resin-rich regions are then represented by a cosine-, orthorhombic- or rectangular shape.

The fiber-reinforced distorted zone has been modelled by a rectangular region in which the fiber direction [34, 35] and the fiber volume fraction [25] are assumed to linearly evolve between the resin-rich region boundaries and the undistorted zone. The out-of-plane undulations (in non-crimp fabrics), which are present due to the small binder yarn, have been modelled by either introducing a locally curved region at the corresponding locations underneath the binder yarn as in [38], or by considering a straight lamina with changes in the local material axis system representing the fiber waviness as in [39, 40]. The stitching yarn is modelled in [10, 23, 36, 37] by straight and circular segments with a circular cross-section in the through-the-thickness segment and an elliptical cross-section in the top segment, and with a full fiber compacted state for each cross-section. The simplified modelling for both stitching yarn and lamina resulted in interpenetrations, which were resolved in the finite element model construction by the adoption of a mesh superposition techniques. An example of a stitching yarn geometry obtained from a micro-CT scan can be found in [41]. The models presented so far in literature can only partially account for the main geometrical features which further highlights the difficulty of using an analytical modelling approach for describing the geometry of deformable stitching yarns incorporating the lamina distortions and the complex shapes of the reins-rich regions that arise for different stitching parameters and stacking sequences.

A computational approach was recently presented to generate unit-cell models of Z-pinned laminates [42]. The resin-rich regions and the pin of the Z-pinned laminates unit-cells were represented by initially straight discretised lines. The discretised lines were shaped by a geometrical inflation, rotation and straightening operations while a geometrical contact treatment accounted for line interactions. The fiber-reinforced distorted zone was modelled on cross-sections of the laminae in a post-processing step, hereby accounting for local variations in the fiber volume fraction and in the fiber direction near the pin due to pin insertion and pin rotation. The computational approach was then adopted and extended for 3D orthogonal woven composites unit-cell models [43], in which a novel inner-line configuration was introduced (similar to the multi-chain digital element configuration used in [44–49] for the generation of 3D woven models) to account for cross-section shape variations of the binder yarn. The computational approach was shown to satisfactorily introduce geometrical features by geometrical operations in the models without incorporating explicitly the mechanics of manufacturing in the model generation.

Here, the computational approach presented in [42, 43, 50] is adopted and further extended for the generation of structural stitched non-crimp fabric composite unit-cell models. The contributions of this manuscript are: (1) the presentation of a novel approach to generate unit-cell models of stitched laminates, including an inner-line configuration for fiber-bundles to account for cross-section deformations, and (2) the generation of unit-cell models including out-of-plane undulations in surface laminae, variations of local fiber-reinforcement distortions near the stitching yarn and a deformable stitching yarn which is conform with the neighbouring lamina. The novelties towards the framework are the introduction of a deformable stitching yarn and a fiber-reinforced distorted zone model for generally shaped cross-sections, and in the analysis of out-of-plane undulations, the presence of the stitching yarn and matrix boundary layer on the stiffness and damage initiation stress-levels.

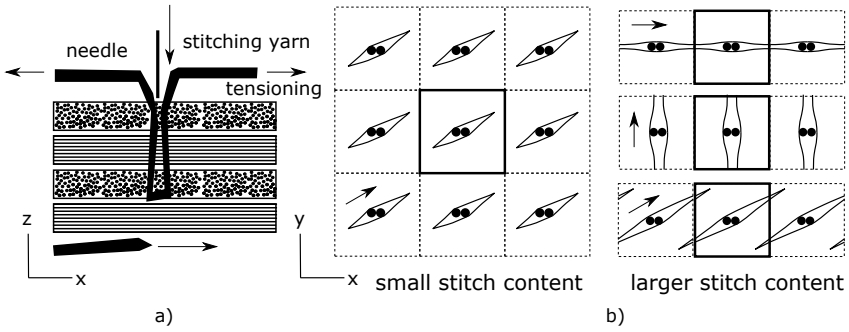

Figure 1: Stitched non-crimp fabric composites: (a) stitching yarn insertion and tensioning, (b) resin-rich regions in a lamina for small and large stitch content and different fiber orientations.

2. Geometrical model generation

2.1. Overview

Unit-cell models of structural stitched non-crimp fabric laminates are generated by a geometry-based framework for different stitching parameters. In this work, a modified lock stitch pattern and a stitch direction along the x-direction are considered for the generated unit-cell models (as illustrated in Fig. 1a). The following assumptions and simplifications are used:

1. The modified lock stitch pattern, which consists of a continuous fiber-bundle located on the bottom and top of a laminate (see Fig. 1a), is simplified represented by two unconnected U-shaped fiber-bundles (see Fig. 2a).
2. The laminae of the non-crimp fabric laminate are assumed to be straight and initially homogeneous in local fiber direction and fiber volume fraction.
3. The minor geometrical features of the binder yarn distortions in the non-crimp fabric laminae, the crimping and the inclination of the through-thickness segment of the stitching yarn, the fiber-weaving for irregular stitch patterns and the broken fibers are not considered in the model generation.
4. The mechanics of the fiber-reinforced regions (such as bending and compaction behaviour) are not considered, but their effect on the geometrical features of the lamina and stitching yarn are accounted for by the geometrical operations.

The experimental data required for the unit-cell model generation are the following:

1. The laminate-stacking sequence, the thickness of each lamina, the initial cross-section dimensions of the stitching yarn, the stitch content and the out-of-plane undulations in the surface lamina are needed to set up the initial unit-cell model. The laminate thickness and the out-of-plane undulations need to be measured in the final stitched laminate, hereby accounting for the effect of transverse compaction on these features in the generated unit-cell models.
2. The length and the width of the resin-rich regions, the amount of stitching yarn tensioning (which correlates with the local deflection of the stitching yarn in its most curved region) and a measure of the flattening of the cross-sections located at the top-segment of the stitched yarn are needed to set the parameters of the geometrical operations.
3. The fiber-volume fraction in the initial undistorted laminae and in the stitching yarn, the maximum local fiber-volume fraction and a local width of the fiber-reinforced distorted zone, are required in the fiber-reinforced region models.

The shape of the geometrical features and the distortions in the fiber-reinforced regions are automatically obtained during the model generation and will be compared with experimental observations presented in Section 4.

As part of the geometrical framework, lines are further used as a tool to shape the geometrical-features of the distorted-lamina and the stitching yarn (as similar to the line-concept being used in [42, 43, 50]). The lines here are considered as three-dimensional geometrical-entities, described by a center-line and cross-section dimensions along this centerline. The term 'lines' is further used to represent these three-dimensional-geometrical entities.

An overview of the unit-cell model generation approach is presented in Fig. 3. The effect of the assumptions and simplifications on the stiffness and damage initiation stress levels are discussed in section 6.2. The same framework can further be extended to generate unit-cell models including other stitching patterns, other stitch-yarn geometry, lamina undulations, as will be part of future work.

2.2. Initial model

The stitching yarn (corresponding to a modified lock stitch pattern) is represented by two U-shaped lines and an initial constant circular cross-section (see Fig. 2a). The U-shaped lines are aligned in the stitch direction (x-direction). Their through-the-thickness segments are positioned near the unit cell center P_C on a very small distance x_{small} from each other and their horizontal parts are positioned on a distance z_1 from the bottom or top of the unit cell. The lines are further discretised in segments with a length equal to one third of a typical stitching yarn diameter ($120\mu m$) [23].

Laminae are represented by initially straight lines that are aligned in their main fiber direction $\vec{f}_{lam}$ (see Fig. 2b-c). The lines are positioned near the through-the-thickness segment of the stitching yarn to represent potential resin-rich regions that arise upon the insertion of the stitching yarn belonging to the unit-cell itself. For inner laminae with fibers not aligned to the main stitch pattern directions, lines are additionally introduced to account for potential resin-rich regions caused by neighbouring stitching yarns (see Fig. 2b). The length of the potential resin-rich regions is hereby limited to the length of the lines that are currently employed to represent the resin-rich regions, where this length can easily be enlarged by adding more lines at corresponding opening locations. For the surface laminae (see Fig. 2c), lines are additionally positioned near the out-of-plane borders of the lamina to account for potential out-of-plane undulations caused

by stitching yarn tensioning. A small line-radius is further attributed to each line (for contact treatment) and the lines are discretised in line segments with a length of $120\mu m$ (similar to the length of the stitching yarn line segments).

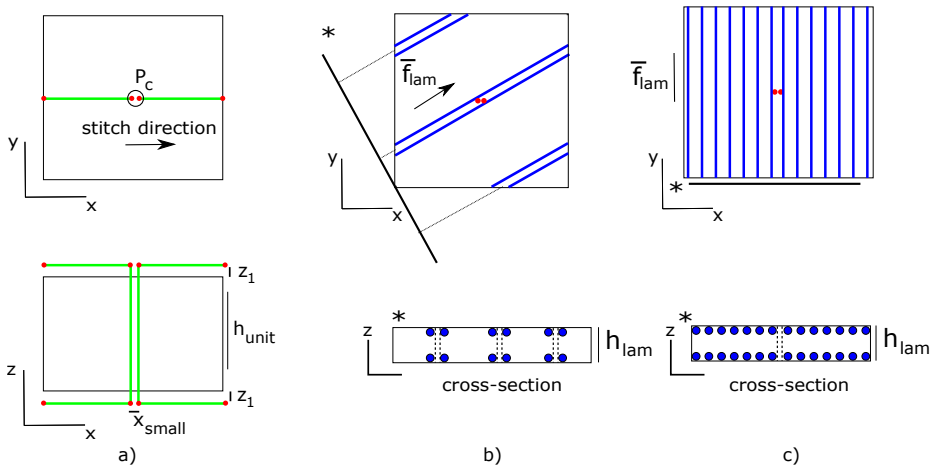

Figure 2: Initial model: (a) stitching yarn model, (b) inner lamina model (lines representing potential resin-rich regions), (c) surface lamina model (lines representing potential resin-rich regions and out-of-plane undulations).

2.3. Geometrical tools

The discretised lines are shaped by geometrical operations in subsequent steps while a contact treatment accounts for line interactions (see Fig. 3). A straightening, a single-line inflation, a multi-line inflation and a flattening operations are considered here as geometrical operations. Each step intends to introduce a geometrical feature in the model or simply transforms the single-line configuration of the stitching yarn into a multi-line configuration (see Table 1). The parameter q_{sl}, which controls the interaction between the stitch lines and lamina lines (see section 2.3.1), is adopted in each step to constrain either the shape of the stitch lines or the lamina lines ($q_{sl} = 0$ and $q_{sl} = 1$ respectively). This constraining allows preserving the geometry of previously generated features, as such to have a larger control over the introduced features, while a periodic straightening operation and displacement boundary conditions applied on the unit-cell in-plane boundaries allow generating in-plane periodic unit-cell models. The step-wise generation process is described in the sequel, followed by a description of the adopted geometrical operations.

Step 1, the stitch lines are inflated by the single-line inflation operation, hereby moving down potentially the lamina lines to account for out-of-plane undulations of the surface lamina in the generated unit-cell model (the out-of-plane undulations are controlled by parameter z_1 in Fig. 2a). The initial circular cross-sections of partially inflated stitching yarns can be transformed into elliptical cross-sections to account potentially for deformable stitching yarns (controlled by parameter f in Eq. 3b, as will be explained in the sequel). During the stitch cross-section transformation, interpenetrations can arise between the stitching yarn and laminae with fibers not aligned transverse on the stitch direction (see Fig. 4). The interpenetrations will further be resolved in step 4 by transforming the single line representation of the stitching yarns into a multi-line representation and by introducing the multi-line representation gradually in the interprenetrated configuration using a multi-line inflation operation.

Step 2, the stitch lines are shaped by the straightening operation to account for different shapes of the stitching yarn centerline due to stitching yarn tensioning

Step 3, the lamina lines are straightened by the same straightening operation to locally smoothen their deformed shapes near the stitching yarn (hereby having constrained the stitch lines).

Step 4, the single-line configuration of the stitching yarn is transformed into a multi-line configuration to account for further cross-section variations of the stitching yarn. The multi-line configuration is further introduced in the model by a multi-line inflation operation to account for the potential interpenetration arising in step 1 and to generate shapes of the stitching yarn conforming with the resin-rich region boundaries (hereby having constrained the lamina lines).

Step 5, a flattening operation is applied on the unit-cell model to mimic the effect of transverse compaction on the cross-sections shapes of the stitching yarn. The lamina-lines are hereby constrained as their geometries were shaped during the previous generation steps.

Step 6, the multi-line configuration of the stitching yarn is tensioned by the straightening operation to account for different cross-section shapes due to stitching yarn tensioning (hereby having constrained the lamina lines).

Step 7, the bottom and top surface of the unit-cell can be adjusted to generate models with a stitching yarn that is fully embedded in the matrix rather than floating on top of the unit-cell.

Step 8, the local fiber volume fraction and fiber direction inside the laminae and the stitching yarn are obtained in a post-processing step.

The parameters of the geometrical operations can be controlled by experimental data (as explained in Section 4). The different steps of the geometrical operations applied attempt to follow further the logic of the stitching process. Indeed, in a stitching process, (1) the stitching yarn is inserted, and the fibers in the lamina are being pushed away, (2) the stitching yarn is tensioned, pushing away further the fibers in the laminae, and shaping the stitching yarn geometry, (3) the laminate is compacted, shaping further the stitching yarn cross-sections. The same logical steps for the operations are adopted in setting the different steps of the generation procedures.

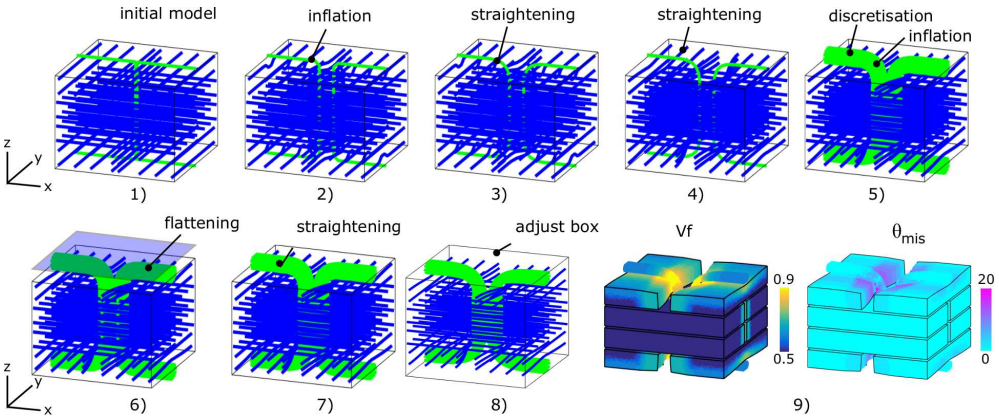

Figure 3: Step-wise generation process: (1) initial model, (2) stitch inflation, (3) stitch straightening, (4) lamina straightening, (5) transformation stitch into multi-line configuration, (6) flattening, (7) stitch straightening, (8) adjusting bottom and top surface of unit-cell box, (9) fiber volume fraction V_f and fiber misalignment θ_{mis} distributions in a post-processing step.

2.3.1. Contact treatment

The contact treatment between two interpenetrating lines is identical to the one presented in [43]. The distance of a line node P to all other lines is evaluated (see Fig. 5). When local interpenetration is detected, the line node P is moved along a direction $\vec{D}_P$ by a fraction q of the interpenetrated distance d_{int} (Eq. 1b). The direction $\vec{D}_P$ in which the node P is moved is the normal from node P onto the other interpenetrated line. The full interpenetration is suppressed by the movement of line node Q which belongs to the other line (see Eq. 1c)). The position of all nodes is updated once all the movements are computed. This procedure is applied iteratively

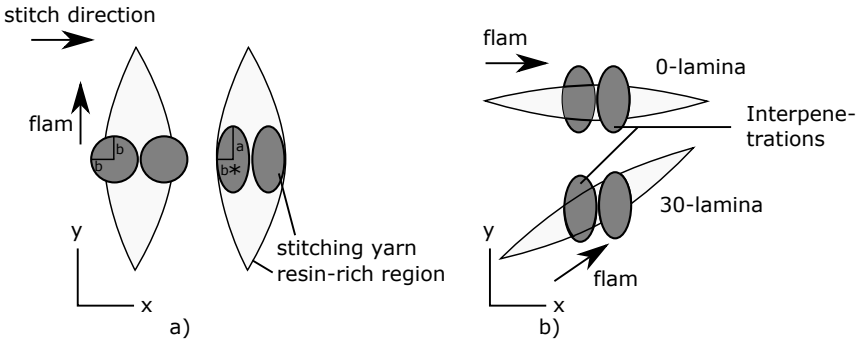

Figure 4: Inflation operation: (a) initial cross-sections transformed into elliptical cross-section for partially inflated stitching yarns, (b) residual interpenetrations in laminae with fibers not aligned in the direction transversal on the stitch direction.

step	operations	id line	q_{sl}	parameter	introduced geometrical feature
1	single-line inflation	stitch	0	f	width of resin-rich region
2	straightening	stitch	0	s_1	centerline of stitching yarn
3	straighening	lamina	1	s_2	length of resin-rich region
4a	multi-line representation	stitch	0	c	deformablility of stitching yarn
4b	multi-line inflation	stitch	0	-	cross-sections of stitching yarn
5	flattening	-	0	z_{limit}	cross-sections of stitching yarn
6	straightening	stitch	0	s_3	cross-sections of stitching yarn
7	adjust box	-	-	no-yes	matrix

Table 1: Different steps during the generation, represented by the applied geometrical operation, a corresponding parameter, the type of line on which the operation is applied, the contact parameter q_{sl} and the geometrical feature which can be used from experimental observations to set the corresponding parameter.

until the maximum interpenetration is below an allowable residual interpenetration distance.

$$d^i_{int} = d^i - (R_1 + R_2) \tag{1a}$$

$$\vec{x}^P_{mov} = q.d^P_{int}.\vec{D}_P \tag{1b}$$

$$\vec{x}^Q_{mov} = (1-q).d^Q_{int}.\vec{D}^Q \tag{1c}$$

where R_1 and R_2 are the radii of the interacting lines, d_i is the distance of point i to the other line, and $\vec{x}^Q_{mov}$ and $\vec{x}^P_{mov}$ are the movements of point P and point Q respectively.

The fraction q, which determines how lines are moved upon interpenetration, is set to be dependent on the type of the interacting lines: two stitch lines are considered to interact symmetrically with each other ($q = 0.50$), lamina lines are allowed to remain interpenetrated ($q = 0.00$), and the interaction between the stitch and the lamina lines is regulated by the fraction q_{sl} which can be set during each generation step to constrain the position of certain types of lines.

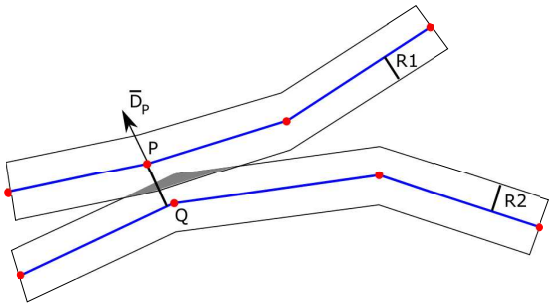

Figure 5: Contact treatment.

2.3.2. *Straightening operation*

Lines are straightened by redefining the position $\vec{x}_i$ of each of their nodes i according to:

$$\vec{x}_i = \frac{1}{2}(\vec{x}_{i-1} + \vec{x}_{i+1}) \tag{2}$$

The operation mimicks the kinematics of a fiber upon tensioning [51, 52]. Small extensions to this implementation are required to account potentially for the effect of distortions in neighbouring unit-cells on the geometry of the lamina and stitch lines. The lines that are straightened (called master-lines in Fig. 6) are therefore extended at both sides by a corresponding part as illustrated in Fig. 6. After straightening, the extended part can be used to update the geometry of slave-lines (see Fig. 6a-b) or be removed (see Fig. 6c).

2.3.3. *Inflation operation*

The inflation operation incrementally increases a line radius R_{line} from 0 to a final radius R_{line}^{final} (Eq. 3a). The final radius is considered as a fraction f of an initial stitching yarn radius

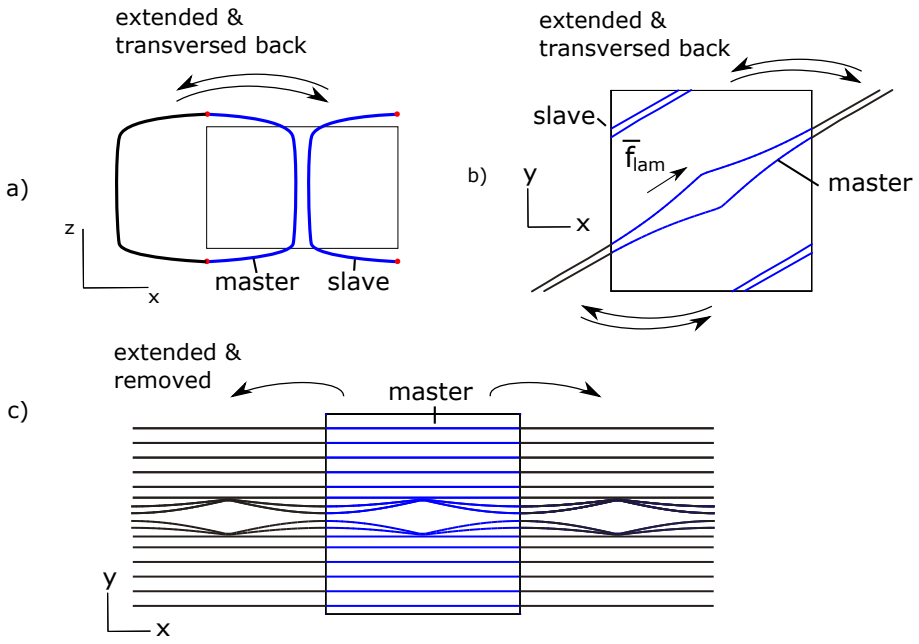

Figure 6: Accounting for the effect of neighbouring unit-cell: (a) the stitching yarn, (b) an inner lamina with fibers not aligned with a stitch pattern direction, (c) a surface lamina.

R_{line}^{init} (Eq. 3b).

$$R_{line}^{n} = R_{line}^{n-1} + \frac{R_{line}^{init}}{n_{infl}} \tag{3a}$$

$$R_{line}^{final} = f.R_{line}^{init} \tag{3b}$$

where n_{infl} is the number of increments required to prevent the stitch lines from jumping over the lamina-lines during the inflation operation. The initial circular cross-sections of partially inflated stitching yarns are subsequently transformed into elliptical cross-sections by extending their transversal dimension on the stitch direction, and by preserving the cross-section area (as was indicated on Fig. 4a).

2.3.4. Inner-line configuration

Fig. 7 illustrates the transformation of the single line configuration of the stitching yarn into a multi-line configuration. The initial cross-sections of the stitching yarn are discretised in circles which are defined by their center points and line radius. The center points are considered as the

points of a uniform triangulation, not be confused with FE nodes and whereby the number of nodes can be regulated by adjusting the uniform mesh size. The line radius R_{line} is determined by the number of lines c and the initial fiber volume fraction $V_{f,stitch}$ of the stitching yarn:

$$R_{line} = \sqrt{\frac{V_{f,stitch}.\pi ab}{\pi c}} \tag{4}$$

where a and b are the long and short axis dimensions of the elliptical cross-section (of the stitching yarn) respectively. The cross-sections are then transformed from the 2D plane configuration into local coordinate systems that are attached to the stitching yarn centerline (see Fig. 7a), whereafter the center nodes of the circles between adjacent cross-sections are connected to obtain the multi-line configuration (see Fig. 7b).

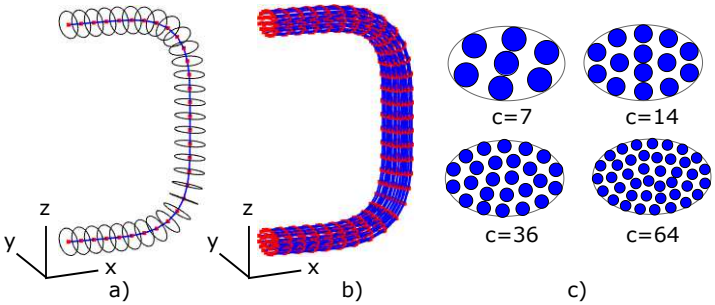

Figure 7: The construction of an inner-line configuration for the stiching yarn: (a) the initial single-line configuration, (b) the multi-line configuration, (c) different cross-section discretisations (c indicates the number of lines.

2.3.5. Multi-line inflation

The multi-line inflation gradually inflates the cross-sections of a multi-line configuration from a reduced size to its original dimensions. It hereby gradually moves the position of the center points in each cross-section away from the stitching yarn centerline and adjusts the radii of the lines. The distance d_{point} of a center point in each cross-section to the cross-section center C, and the corresponding direction $\vec{D}_{point}$ (see Fig. 8a), are first determined:

$$d_{point} = ||\vec{x}_{point} - \vec{x}_C|| \tag{5a}$$

$$\vec{D}_{point} = (\vec{x}_{point} - \vec{x}_C)/d_{point} \tag{5b}$$

The position of each center node $\vec{x}_{point}$ and the radius R_{line} of each lines can then be incrementally updated according to:

$$\vec{x}^{i}_{point} = \vec{x}_C + (\frac{i}{n}).d_{point}.\vec{D}_{point} \tag{6a}$$

$$R^{i}_{line} = (\frac{i}{n}).R_{line} \tag{6b}$$

where i is the increment number. The number of increments n should be large enough to prevent the crossing of the stitch lines over the lamina lines during the multi-line inflation operation:

$$\left(\frac{max(d_{point})}{n}\right) < (R^{lam}_{line} + R^{stitch}_{line}) \tag{7}$$

where R^{lam}_{line} and R^{stitch}_{line} are the radii of the lamina lines and stitch lines, respectively. An example of the stitching yarn and its cross-section at different stages during the multi-line inflation operation is illustrated in Fig. 8b.

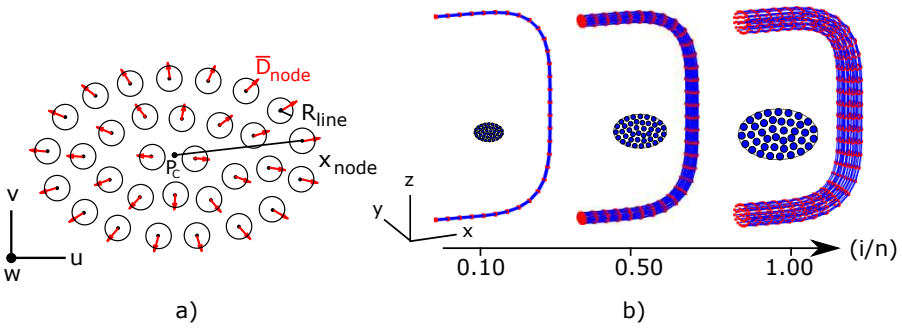

Figure 8: Multi-line inflation operation: (a) a discretised cross-section (b) different inflation levels of the stitching yarn.

2.3.6. Flattening operation

A top boundary vertical position is gradually decreased from z^{init}_{limit} to z^{final}_{limit} while lines coming into contact with this border are moved to the corresponding position (see Fig. 9). The self-contact between the lines is processed by the contact treatment.

2.3.7. Boundary conditions

Displacement constraints are applied on the nodes that are located on unit-cell borders, to keep the unit-cell borders straight and periodic, and on the bottom of the surface laminae to keep the bottom straight. The displacement constraints are enforced by moving the nodes geometrically

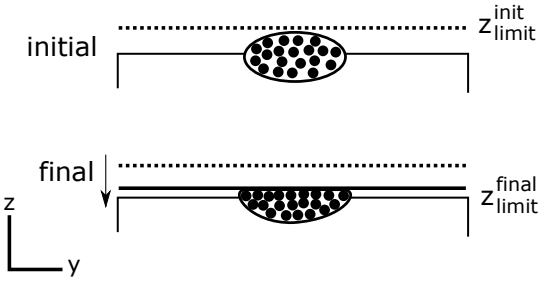

Figure 9: Flattening operation whereby a vertical limit z_{limit} is gradually lowered.

from the specific locations (unit-cell borders, bottom of surface lamina) after each iteration step back to their intended position.

2.4. Fiber-reinforced distorted zone model in lamina

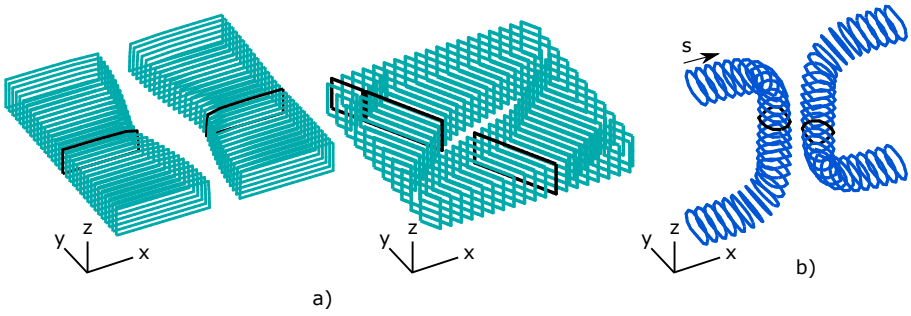

Figure 10: Generated cross-sections for: (a) surface and inner laminae, (b) the stitching yarn.

The fiber-reinforced distorted zone and the corresponding local fiber volume fraction and fiber direction are modelled on cross-sections in the lamina (as illustrated in Fig. 10a). The cross-sections are obtained from the discretised lines by intersections perpendicular to the main fiber direction in the lamina and by accounting afterwards for the line radius of the lamina lines. The fiber-reinforced distorted zone in each cross-sections is assumed to take place only in a limited region near the deformed border of the cross-section. The width of the fiber-reinforced distorted zone in each cross-section is furthermore considered to be dependent on the local movement of the border (see Fig. 11a). Local distorted zones near each line in a cross-section will therefore first be constructed and then combined into a global distorted zone.

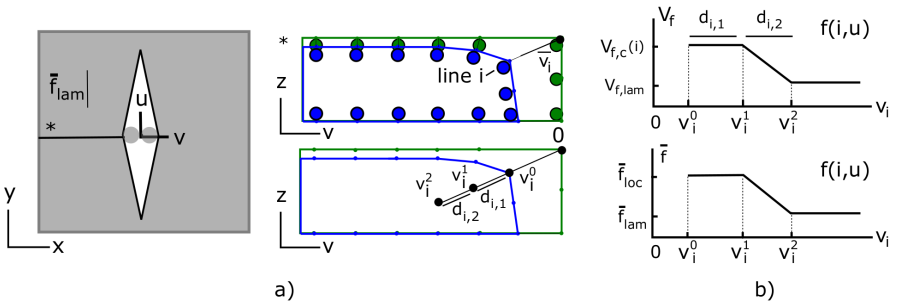

Figure 11: Local distorted zone model near a line in a cross-section: (a) an undeformed and deformed cross-section (green and blue respectively) indicating the model parameters (the circles in the top cross-section represent the intersections of the discretised lines at the cross-section location), (b) the assumed fiber volume fraction V_f and fiber direction $\vec{f}$ distribution near a line in cross-section along a local axis v_i.

2.4.1. Distorted zone near a line in a cross-section

The distorted zone near a line i in a cross-section at position u (see Fig. 11a) can be characterised by two regions with different fiber volume fractions and fiber direction distribution, similar to concepts presented in [42]. The first region, which is the closest to the deformed border, is characterised by a constant but increased fiber volume fraction $V_{f,c,i}(u)$ and a constant fiber direction $\vec{f}_{loc}(u,i)$ that is tangent to the boundary of the resin-rich regions or at the top surface of the lamina. The second region, which is located between the first region and the undistorted zone, is characterised by a fiber volume fraction and a fiber direction linearly evolving between both regions. The widths of these first and second region in a cross-section at position u near a line i are represented by $d_{i,1}(u)$ and $d_{i,2}(u)$ respectively.

The parameters $d_{i,1}(u)$, $d_{i,2}(u)$ and $V_{f,c}(u,i)$ are computed based on the following assumptions. First, an amount of fibers that is equivalent to $v_i(u).V_{f,\text{lam}}$ is assumed to be redistributed locally according to [42]:

$$v_i(u).V_{f,\text{lam}} = (d_{i,1}(u) + \frac{d_{i,2}(u)}{2}).(V_{f,c,i}(u) - V_{f,\text{lam}}) \tag{8}$$

where $v_i(u)$ is the movement of the line i at position u and $V_{f,\text{lam}}$ is the initial fiber volume fraction in the lamina. Secondly, $d_{i,1}(u)$ and $d_{i,2}(u)$ are assumed constant along each line i. Thirdly, $d_{i,1}$

is considered a multiplication of $d_{i,2}$:

$$d_{i,1} = k.d_{i,2} \tag{9}$$

where k is considered equal for each line.

The local fiber volume fraction in the lamina near the stitching yarn is assumed to depend linearly on the local movement of the stitching yarn and is assumed to be equal to the maximum fiber volume fraction $V_{f,max}$ for local movements of the stitching yarn larger than d_{max}:

$$V_{f,i} = V_{f,lam} + \frac{v_{i,max}}{d_{max}}.(V_{f,max} - V_{f,lam}) \quad \leq V_{f,max} \tag{10}$$

where $v_{i,max}$ represents the local movement of the stitching yarn locally near a line i and is determined from the maximum displacement v of the line i. The maximum local fiber volume fraction $V_{f,max}$ is considered to be 0.9, representing the fiber volume fraction of a fully packed hexagonal fiber-configuration [53]. The distance d_{max} is considered $100\mu m$, being approximately 10 times a carbon fiber diameter. The system of equations is then solved by first computing the increased fiber volume fraction $V_{f,c,i}(u)$ in the cross-section underneath the stitching yarn (using Eq. (10)), followed by the calculation of $d_{i,1}$ and $d_{i,2}$ using Eq. (8)-(9), from which afterwards $V_{f,c,i}(u)$ can be computed for each line i at each cross-section position u.

The values of the distorted zone parameters are then assigned to circular-shaped distorted zones as illustrated in Fig. 12a. The fiber volume fraction $V_{f,i}$ and the fiber direction $\vec{f}_{loc,i}$ distributions near a line i in a cross-section at position u for such circular-shaped distorted zones can be described as:

$$V_{f,i}(r,u) = \begin{cases} V_{f,lam} & (d_{2,i} \leq r) \\ V_{f,lam} + (\frac{r-d_{1,i}}{d_{2,i}-d_{1,i}})(V_{f,c,i}(u) - V_{f,lam}) & (d_{1,i} \leq r \leq d_{2,i}) \\ V_{f,c,i}(u) & (r \leq d_{1,i}) \end{cases} \tag{11}$$

$$\vec{f}_{loc,i}(r,u) = \begin{cases} \vec{f}_{lam} & (d_{2,i} \leq r) \\ \vec{f}_{lam} + (\frac{r-d_{1,i}}{d_{2,i}-d_{1,i}})(\vec{f}_{border,i}(u) - \vec{f}_{lam}) & (d_{1,i} \leq r \leq d_{2,i}) \\ \vec{f}_{border,i}(u) & (r \leq d_{1,i}) \end{cases} \tag{12}$$

where r is the distance from a point to the point center C_i corresponding to line i.

2.4.2. *Distorted zone in a cross-section*

The global fiber volume fraction field $V_f(u, v, z)$ is determined in each cross-section by taking locally the maximum of the local fiber volume fraction fields $V_{f,i}$:

$$V_f(u, v, z) = max(V_{f,i}(r, u))$$

The global fiber direction field $\vec{f}_{loc}(u, v, z)$ is defined in each point of a cross-section as the local fiber direction belonging to the line i from which the fiber volume fraction was obtained:

$$\vec{f}_{loc}(u, v, z) = \vec{f}_{loc,i}(u, v, z) \quad \text{with } i \text{ satisfying} \quad V_f(u, v, z) = V_{f,i}(u, v, z)$$

The fiber misalignment θ_{mis}, which is often used in the illustrations to represent the fiber direction in a lamina, is defined by the angle between a local fiber direction and the main fiber direction in the lamina. Examples of obtained fiber volume fraction, and in-plane, out-of-plane and total fiber misalignment distribution in a cross-section are illustrated in Fig. 12b.

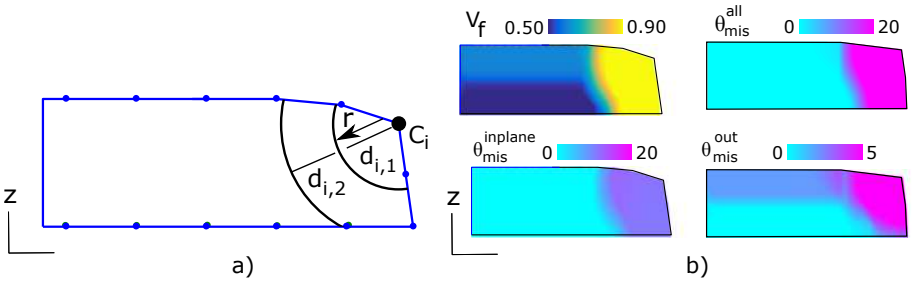

Figure 12: Distorted zone model in a cross-section: (a) a circular-shaped local distorted zone near each line, (b) the obtained fiber volume fraction V_f and fiber misalignment θ_{mis} distribution, as well as the in-plane and out-of-plane fiber misalignment distribution (θ_{mis}^{in} and θ_{mis}^{out} respectively).

2.5. *Fiber-reinforcement model in the stitching yarn*

A constant fiber volume fraction and fiber direction are assumed in each cross-section of the stitching yarn (which was illustrated in Fig. 10b). The constant fiber volume fraction in a cross-section at position s along the stitching yarn is determined as:

$$V_f(s) = \frac{A_{init}}{A_{deform}(s)} . V_{f,stitch} \tag{13}$$

where A_{init} and A_{deform} are the initial and deformed area of the cross-section, respectively, and $V_{f,stitch}$ is the initial local fiber volume fraction of the stitching yarn. The constant fiber direction in each cross-section is taken as the local tangent to the centerline at the cross-section position.

3. Reference material geometry

The reference material geometry is considered here to be a 4-layer laminate that is structural stitched, with the following parameters:

1. The laminate has a stacking sequence [0/90/90/0], with an assumed initial homogeneous fiber volume fraction in each lamina of 0.500 (similar with [3]) and a lamina thickness of each equal to $300\mu m$ (similar to [35]).
2. The stitching yarn has an initial fiber-volume fraction of 0.500 and an initial circular cross-section diameter of $0.100mm$ (conform with [23]).
3. A stitch content of 2% has been adopted which results in unit-cell-dimensions of 1750x1750νm.

The size of the geometrical features in the lamina and the stitching yarn are varied using the parameters of the geometrical operation (see Section 4). The shapes of the geometrical features corresponding to the geometrical parameters variations is validated by experimental observations. A summary of the experimental data which are further used in the geometrical model generation section and the mechanical simulation section, is presented in Table 1. The charts obtained by varying the parameters of the geometrical operations (see Section 4) can then be used to set the value of these geometrical operation parameters in the generation of unit-cell models for specific specimens corresponding to defined stitching parameters. An in-depth one-to-one comparison of experimental specimens with models for different stitching parameters will be considered in a future work.

4. Generation of geometrical features

Unit-cell models with different values for the geometrical operation parameters are generated to illustrate the possibilities of the framework to generate unit-cell models including geometrical features corresponding to different stitching parameters. The generated geometrical features are qualitatively compared with trends obtained from experimental figures. The graphs, which are relating the geometrical operation parameters with the size of geometrical features and which are obtained from the generation process (see following sections), can be used to set the parameters according to experimentally obtained features.

4.1. Centerline of the stitching yarn

Different shapes of the stitching yarn's centerline can be obtained by varying the number of straightening operations s_1 or the contact parameter q_{sl} in generation step 3. In Fig. 13a, the parameter s_1 is varied while having set q_{sl} equal to 0. In Fig. 13b, the parameter q_{sl} is varied while having set s equal to 10. The parameter s_1 increases the main deflections of the centerline while the parameters q_{sl} fine-tunes its shape in the highest curved region. The shapes of the stitching yarn centerlines compares satisfactory with experimental observations presented in [3, 9].

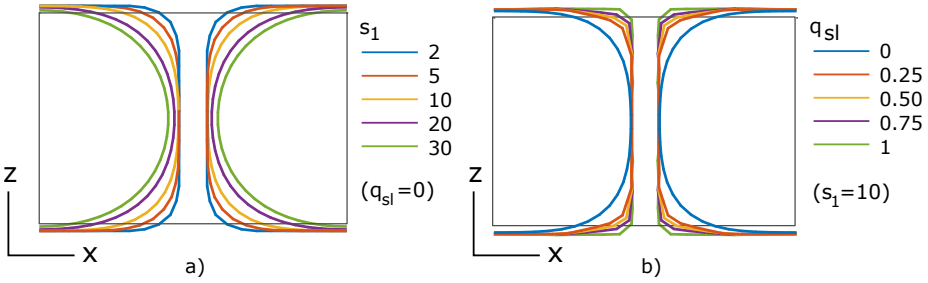

Figure 13: Different shapes of the stitching yarn centerline by varying: (a) the straightening parameter s_1 and (b) the contact parameter q_{sb}.

4.2. Shapes of the resin-rich regions

The complexity in shapes of the resin-rich regions for different laminate stacking sequences and stitch content, which can automatically be generated in step 2, is illustrated in the following (Fig. 14). A [90°/0°/30°/90°] stitched laminate with a stitching yarn initial radius of 100μm is considered. The unit-cell size is taken as either 3550μm or 1770μm for a stitch content of 0.5% or 2% respectively. In Fig. 14, the seamless transition from an eyelet-shaped into a smooth channel shaped resin-rich region for increased stitch content can be obtained. The width of the resin-rich regions that depends on the angle between the fiber direction in the lamina and the stitch direction is also captured; and the asymmetrical shapes of the resin-rich region and fiber misalignment distributions in lamina with fibers not aligned in stitch pattern direction are also obtained. The eyelet-shaped and channel-shaped resin-rich regions, and the widening-shapes of the resin-rich regions near surface lamina can also be observed in [9, 23].

4.3. Cross-section shapes of the stitching yarn

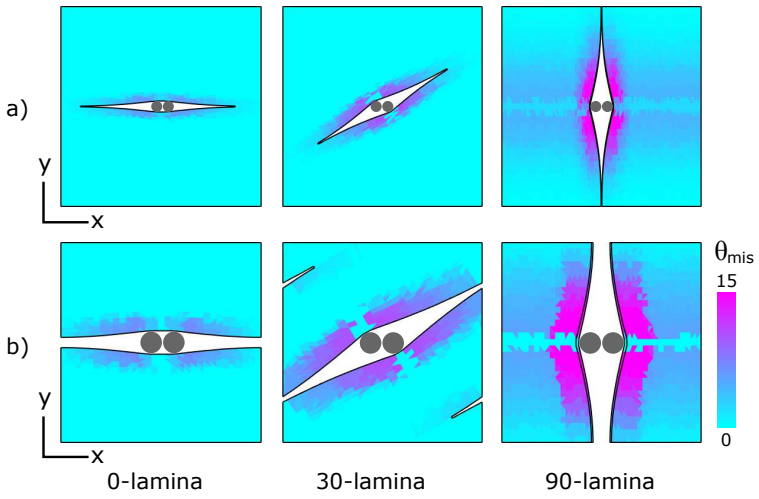

Figure 14: An illustration of the shapes of resin-rich regions and fiber misalignment distributions θ_{mis} in stitched laminae for different orientations of the main fiber direction (0°, 30° and 90°) in the lamina and different stitch content: (a) a stitch content of 0.50%, (b) a stitch content of 2.00%.

First, the number of lines in the multi-line configuration (parameter c in Eq. (7)) is determined by a convergence study on the geometry of a stitching yarn on which a certain number of straightening operations were applied. Afterwards, the cross-section shapes of the stitching yarn for a different number of straightening operations applied on the stitching yarn mimicking different stitching yarn tensioning stages, are illustrated.

4.3.1. Convergence study on the number of lines

Fig. 15 illustrates the effect of using a different number of lines c (in generation step 4) on the geometry of a tensioned stitching yarn. Cross-section discretisations with 7, 14, 36, and 64 lines were analysed and the effect of the number of lines was investigated on the deformed shapes and area of the cross-sections located at given positions along the stitching yarn (see Fig. 15a). It can be seen that the shape and area of the considered cross-sections converges and that this convergence is already taking place for a number of lines equal to 14. So, c equal to 14 is used in further model generations (see Table 1).

4.3.2. Mimicking different stitching yarn tensioning

Cross-section shape variations in the stitching yarn corresponding to different stitching yarn tensioning states can be generated by setting a different number of straightening operations s_3 in step 5 (see Fig. 16a). The cross-sections in the most curved region (plane 2) are the most affected by increasing the value of s_3, while the cross-sections in the through-thickness (plane 4) are barely affected by this parameter. The latter can be explained from the highly compacted states of the multi-line configuration in the through-thickness segment of the stitching yarn due to multi-line inflation process (see Fig. 15), with a fully compacted state in the through-the-thickness segment of the stitching yarn also being considered in the analytical models presented in [53]. More compacted states of the stitching yarn can further be observed from the fiber volume fraction distribution contour plots presented in Fig. 16b for increasing values of s_3. The more compacted state in the curved segment of the stitching yarn can be observed in [41], while the gradual reduction in cross-section dimensions and the flattening of cross-section in the top-segment can be observed in [3].

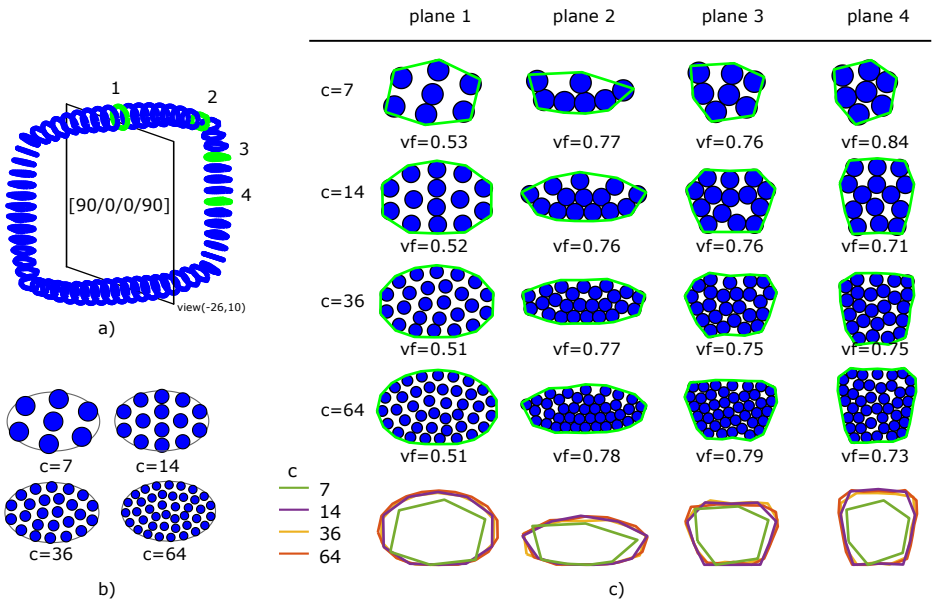

Figure 15: Convergence study for the number of lines c on the geometry of a tensioned stitching yarn: (a) the cross-section locations, (b) the initial cross-sections corresponding to different lines, (c) the deformed cross-section shapes and local fiber volume fraction.

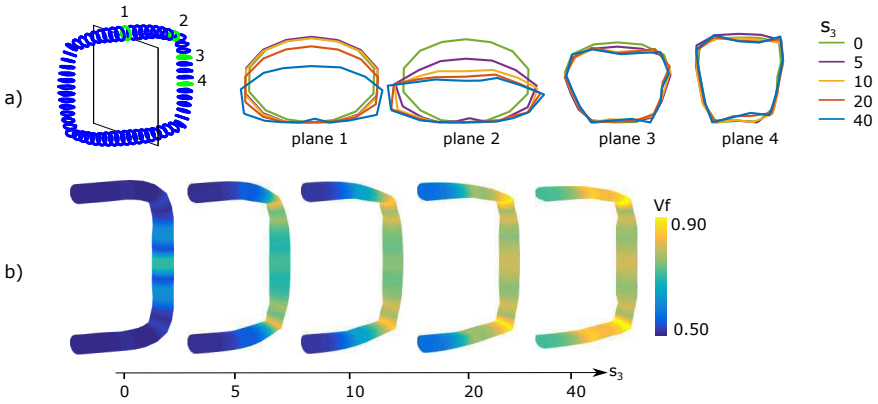

Figure 16: Shapes of a tensioned stitching yarn for varying straightening parameter s_3: (a) cross-section shapes and (b) fiber volume fraction V_f distribution.

5. Mechanical simulations

The geometrical models can afterwards be transformed into FE-based unit-cell models using the procedures as presented in [50]. The unit-cell models are subjected to periodic boundary conditions on their in-plane borders while their bottom and top surfaces remain free. Carbon fibers and epoxy matrix are considered as constitutive materials for which properties are presented in Table 2. The properties of the fiber-reinforced region in function of the local fiber volume fraction are obtained using the Chamis-formulae [54] (for stiffness) and emperical formulae presented in [55] (for strength) in which the local fiber direction is used to define the local material axis-system in which these properties are assigned. A global strain of 0.50% is then applied on the unit-cell model, a straining level that has been shown experimentally to cause early damage initiation in stitched laminates [10, 16].

A global strain of 0.50% is applied on the unit-cell to compute its stiffness and to assess the presence of regions in which damage may be initiated caused by the geometrical imperfections at this strain-level relative to an unstitched reference laminate. Linear elastic simulations has been used during the assessment, with the intention to capture changes in stiffness and stress concentrations relative to the unstitched laminate. Non-linear materials models and non-linear simulations, required to predict complete failure and thereby the strength of the unit-cell models, will be part of future work.

Additionally, the mesh size parameters (as presented in [50]) have been assessed using a mesh-convergence study on the stiffness and on the damage initiation indicators (which are described in section 5.1). The number of mesh elements depends on the size of the unit-cel model, which is correlated with stitching-yarn spacing, and the mesh size parameters. A minimum mesh size of $15\mu m$ was taken in the locally refined regions in-between the lamina and between the lamina and stitching yarn, which has been taken equal to the gap between these geometrical-entities introduced during the geometrical unit-cell model generation to facilitate subsequent mesh generation (see [50]).

The order of magnitude for the number of elements is in the order of 10^5. The order of magnitude for the computational time to perform both the geometrical model generation and the subsequent mechanical simulation is in the order of minutes.

Stiffness	carbon fiber	epoxy matrix	strength	carbon fiber	epoxy matrix	interface
$E_{11}(GPa)$	231	3.45	$X_{11,t}(MPa)$	3500	70	-
$E_{22}(GPa)$	15	-	$X_{11,c}(MPa)$	3000	130	-
$E_{33}(GPa)$	15	-	$X_{12}(MPa)$	-	57	-
v_{12}	0.20	0.35	$\epsilon^f_{11,t}(\%)$	1.51	4.5	-
v_{13}	0.20	-	$\epsilon^f_{11,c}(\%)$	1.30	8	-
v_{23}	0.20	-	$\gamma^f_{12}(\%)$	-	5	-
$G_{12}(GPa)$	15	1.28	$X_{nn}(MPa)$	-	-	80
$G_{13}(GPa)$	7	-	$X_{nt}(MPa)$	-	-	100
$G_{23}(GPa)$	7	-				

Table 2: The stiffness and strength properties of carbon fiber (type AS4 [56]) and epoxy matrix (type 5260 [56]), and the strength properties of the interface between the fiber-reinforced regions and the matrix [57].

5.1. Analysis methodology

The mechanical simulations performed in this work are linear-elastic and the local damage initiation levels are evaluated by simple maximum stress-criteria. The stiffness of the unit-cell models is computed and normalised by the stiffness of the equivalent unstitched laminate model.

The local stress-levels are evaluated based on their risk to locally initiate damage. Transverse and shear damage in the fiber-bundles (via f_{22} and f_{12} respectively), interface debonding between the fiber-bundles and the matrix (via f_{int}), and matrix damage (via f_m) are considered in the analysis, as being the ones which can potentially arise (stated by the experimental observations presented in [58, 59]). The damage initiation indicators (f_{ij}, f_{int}, f_m) are calculated by the maximum stress-based criteria presented in [43]. A 97-percentile of the damage initiation indicators f_{ij} (see [43]) is used ($f_{ij}^{97\%}$) to compare the potential local damage initiated regions between different models. Damage initiation indicators reaching values above one ($f_{ij} > 1$), indicates the occurance of damage initiation. The simple maximum stress-criteria can be extended by more elaborated damage-based models (Puck [60], Hashin [61]) for future strength predictions.

laminate	stacking sequence	$[0°/90°/90°/0°]$
	$V_{f,lam}$	0.500
	unit-cell dimensions	$1750x1750x1200\mu m^3$
	ply thickness	$300\mu m$
stitching yarn	radius	$100\mu m^*$
	$V_{f,stitch}$	0.500
	content	2%
	spacing	$1750\mu m$
generation parameters	$f = 0.80$, $s_1 = 7$, $s_2 = 50$, $s_3 = 7$, $k = 1$,	adjust box = no

Table 3: The initial model and generation parameters for the stitched laminate model. The radius of the stitching yarn is calculated from the stitching yarn spacing, the stitch content and an assumed initial circular cross-section of the stitching yarn.

5.2. Models

The effect of stitching, local fiber volume fraction distribution and fiber misalignment, and geometrical model simplifications on the stiffness and local stress concentrations is analysed by the following three cases, using models which are geometrically characterised in Table 4:

1. Case 1: the stitched laminate model (Fig. 17a)(model 7) is compared with an equivalent unstitched laminate model (model 1) to investigate the effect of stitching. The stitched

laminate model is generated using the generation procedures and parameters as described in Table 1 and Table 3, respectively. The unstitched laminate model is taken as the initial model without the stitching yarn and the corresponding distortions on the reinforcement architecture.

2. Case 2: the fiber volume fraction and fiber direction distribution in the lamina can be considered either constant or variable to investigate the influence of fiber volume fraction and fiber direction variations (models 2-5). The constant fiber volume fraction $V_{f,const}^{lam}$ in each lamina is hereby obtained by accounting for the resin-rich regions, while the constant fiber direction $\vec{f}_{loc}$ in each lamina is the main fiber direction $\vec{f}_{lam}$ in the lamina.

3. Case 3: the stitched laminate model is compared with three simplified geometrical models (Fig. 17b-d). The simplifications made in the models are a consequence of: not including a stitching yarn (Fig. 17b), not including the stitching yarn and out-of-plane undulations (Fig. 17c), and considering a matrix surrounding the whole unit-cell model (Fig. 17d). For the straight-border model, the surface lamina bottom and top boundaries were constrained during the generation.

model	description	$V_f^{lam,xy}$	$V_{f,surf}^{max}$	$(\theta_{mis} > 0)_{surf}^{vol\%}$	$\theta_{mis,xy}^{max}$	$\theta_{mis,z}^{max}$	θ_{mis}^{max}
1	equivalent	0.46	0.50	0.00	0	0	0
2	const V_f / const $\vec{f}_{loc}$	0.46	0.72	0.00	0	0	0
3	var V_f / const $\vec{f}_{loc}$	0.44	0.90	0.00	0	0	0
4	const V_f / var $\vec{f}_{loc,xy}$	0.46	0.72	0.37	12	0	12
5	const V_f / var $\vec{f}_{loc,z}$	0.46	0.72	0.57	0	6	6
6	var V_f / var$\vec{f}_{loc}$	0.44	0.90	0.64	12	6	13
7	no stitch	0.44	0.90	0.64	12	6	13
8	straight border	0.46	0.90	0.37	12	0	12
9	box around	0.36	0.90	0.65	12	6	13

Table 4: The in-plane fiber volume fraction V_f and geometrical characteristics in the surface lamina for the different models.

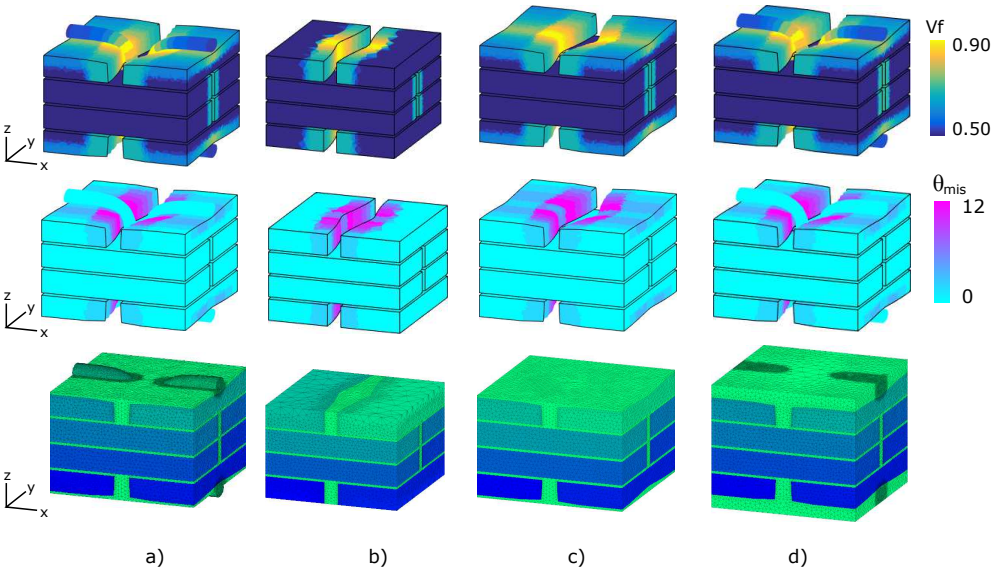

Figure 17: Different models illustrated by means of the fiber volume fraction V_f and fiber misalignment θ_{mis} distribution, and the generated mesh: (a) stitched laminate model, (b) no stitching yarn model, (c) straight border model, (d) box around model.

5.3. Results

5.3.1. The effect of stitching (case 1)

The normalised stiffness of the stitched laminate model in the x- and y-direction is 1.01 and 0.85 respectively. The stiffness in the x-direction is slightly increased, while the stiffness in the y-direction is largely decreased. The decrease in stiffness can be attributed to the fiber misalignments, that are larger in the fiber-reinforced regions aligned in the y-direction, where the slight increase in stiffness can be attributed to the presence of the stitching yarn. These results agree with the experimental data presented in [11] which show the normalised stiffness to vary in between 0.80 and 1.20.

The local damage initiation indicators in the stitched laminate model for x- and y- loading are summarised by their 97-percentile value in Table 5. The 97-percentile of the damage initiation indicators is increased by a factor 2 to 3 in the lamina. Some indicators becoming above one ($f_{ij} > 1$) when stitched, indicating early damage initiation. Transverse cracking in the surface lamina is present for the x-loading, and shear cracking in the surface lamina and transverse

cracking in the stitching yarn are present for the y-loading, with the locally failed regions (see Fig. 18) being situated near the stitching yarn. The stitching yarn experiences hereby damage for y-direction loading but not for x-direction loading. Note that the damage initiation regions are symmetrically on bottom and top of the laminate, while in physical models, the knot configuration of the stitching yarn may cause increased levels of distortions and corresponding damage initiated regions at the bottom of the laminate.

		stitch			surface lamina		inner lamina		interface	matrix
		$f_{22}^{97\%}$	$f_{12}^{97\%}$	$f_{int}^{97\%}$	$f_{22}^{97\%}$	$f_{12}^{97\%}$	$f_{22}^{97\%}$	$f_{12}^{97\%}$	$f_{int}^{97\%}$	$f_{m}^{97\%}$
x-load	equivalent	-	-	-	0.49	0.00	0.12	0.00	0.00	0.28
	var V_f/var $\vec{f}_{loc}$	0.30	0.38	0.75	0.94	0.49	0.25	0.27	0.13	0.63
y-load	equivalent	-	-	-	0.12	0.00	0.49	0.00	0.00	0.28
	var V_f/var $\vec{f}_{loc}$	1.85	0.12	0.64	0.85	1.70	0.84	0.08	0.38	0.56

Table 5: A 97-percentile of the local damage initiation indicator distributions in the equivalent unstitched and stitched laminate model.

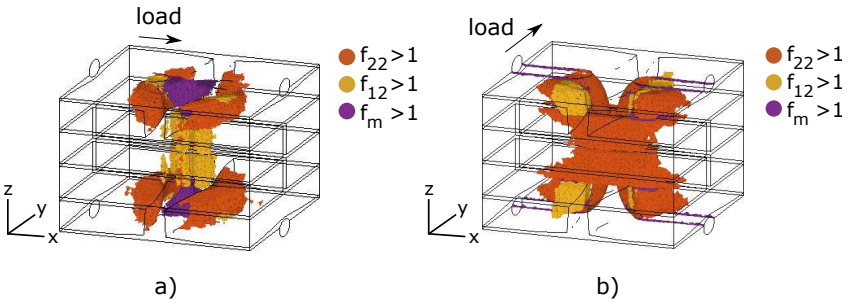

Figure 18: Locally failed regions in the stitched laminate model for different load directions: (a) in the stitch direction, (b) transverse on the stitch direction.

5.3.2. The role of fiber volume fraction and fiber misalignment (case 2)

The influence of fiber volume fraction and fiber misalignment variations on the normalised stiffness and damage initiation for the stitched laminate model is illustrated in Fig. 19. The normalised stiffness in the y-direction $E_{norm,y}$, and the local damage initiation indicators $f_{22}^{97\%}$ and $f_{12}^{97\%}$ in the surface lamina for x- and y-loading respectively, are considered in the analyses, as

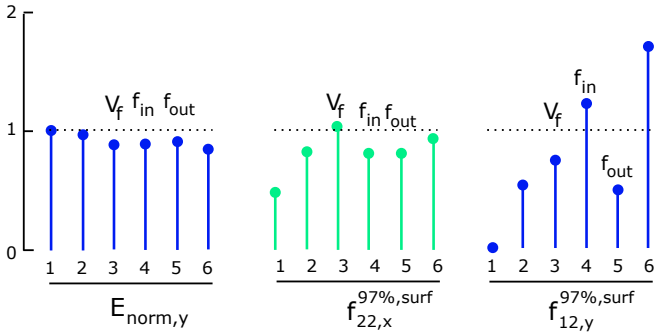

Figure 19: The role of local geometrical features on the stiffness and local damage initiation indicators for the models presented in Table 4.

these parameters have been shown to be the most affected by stitching (see case 1). The following can be observed (see Fig. 19): The normalised stiffness in the y-direction is evenly affected by both fiber volume fraction and fiber misalignment variations. Transverse cracking in the surface lamina $f_{22}^{97\%}$ is mainly affected by the fiber volume fraction (as in experimental observations reported in [17]). Shear cracking in the surface lamina $f_{12}^{97\%}$ is mainly affected by the (in-plane) fiber misalignment. Therefore, it is important to include the local fiber volume fraction and the fiber misalignment in the models in order to predict correctly damage initiation.

5.3.3. The effect of geometrical simplifications (case 3)

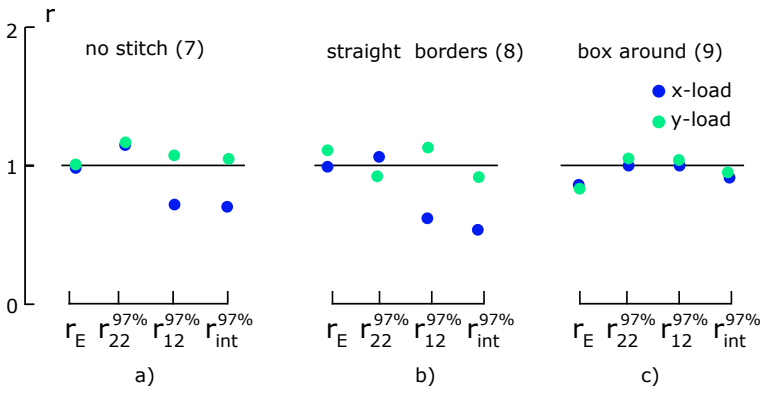

Figure 20: The effect of geometrical model simplifications on the stiffness and local damage initiation indicators for the models presented in Table 4: (a) no stitching yarn model, (b) straight border model and (c) box around model (r represents the parameters of model, normalised by the corresponding parameters of the full stitched model).

The effect of simplified geometrical features on the stiffness and damage initiation indicators in the surface lamina of the simplified models for x- and y-loading is illustrated in Fig. 20. The stiffness and local damage initiation indicators of the simplified models are here normalised by corresponding parameters of the stitched laminate model. The following can be observed (see Fig. 20). A model which does not include the stitching yarn (model 7 in Table 4) can provide a good estimate for the stiffness but underestimates or overestimates the local damage initiation indicators in the surface lamina. A model which does not include the stitching yarn nor the out-of-plane undulations in the surface lamina (model 8 in Table 4) overestimates the stiffness in the y-direction, and underestimate and overestimate even more the local damage initiation indicators compared to a model which does not include the stitching yarn. A model which embeds fully the stitching yarn (model 9 in Table 4) underestimates the stiffness but can still provide a satisfactory estimation of the local damage initiation indicator with respect to the full laminate model. Both stitching yarn, out-of-plane undulations and a matrix region which surrounds only the in-plane fiber-reinforced regions should therefore be considered in models aiming at an accurate prediction of both the stiffness and the damage initiation stress levels.

6. Discussion

6.1. Geometry-based framework compared with FE-simulations

The geometry-based framework offers a fast, simple and straightforward way to include complex-shaped geometrical-features in unit-cells models. The shape of the geometrical features are introduced automatically in the unit-cell models using a step-wise process in which the shape of each geometrical feature is introduced separately. The size of the geometrical-features, as being obtained from experimental-data, can be used in setting model-parameters. The geometrical operations and the geometrical boundary conditions render the unit-cell model generation to be in the order of minutes, which allows for parametric studies. The framework does not include the mechanics of fiber-reinforced regions or the manufacturing processes, but it was shown that it predicts satisfactory shapes of geometrical features for different stitching parameters including an automated post-processing of the lines into finite element models using tools presented in [50].

Finite-elements similuation tools could also be used to build unit-cell models of structural stitched composites, similarly to the digital element technique which is used for unit-cell model

generation in 3D woven composites (see [44–49]). The fiber-reinforcement in the lamina and the stitching yarn will need to be represented by virtual fibers, modelled beam or rod-elements with an enhanced fiber-radius to make the FE-simulations computationally feasible. The stitch insertion, stitch tensioning and transverse compaction can then explicitly be accounted for. An explicit FE-simulation should be adopted and special unit-cell boundary constructions should be constructed (which may be similar to [46, 62]) to preserve periodicity during the unit-cell model generation. Such FE-simulations then include to a certain extent the mechanics of the manufacturing process, but they have been shown to be time-consuming for 3D woven-composites. They are also non-fully predictive by requiring experimental data to fit the mechanical parameters of the virtual fibers. Furthermore, the size and the shape of the geometrical features cannot explicitly-controlled, which reduce the applicability for accurate geometrical model generation.

6.2. The model assumptions

The continuity and the knot-structure of the stitching yarn, the potential undulated-lamina due to stitch insertion and transverse compaction, and minor geometrical features in the laminae are not considered in the unit-cell-model generation (see section 2.1). The effect of these assumptions on stiffness and damage initiation stress levels can be the following:

1. The knot-structure may cause a slight increase of the stiffness in the stitch direction (due to the horizontal continuity of the stitching yarn segments) and enhanced stress-concentrations in the fiber-reinforced regions at the bottom-up of the laminate (due to the larger knot). On one hand, the underestimation of the stiffness may however be limited due to the fact that (1) the stitching yarn is only a small fraction of the in-plane fiber-volume fraction in the stitch direction and (2) that it has been shown that the presence of the stitching yarn affects barely the stiffness (see Fig. 20 a). On the other hand, the potential increased stress concentrations are assumed to be in the same range of the other model simplifications (being no fiber-breakage, asymmetry of stitching yarn, fiber-weaving between stitch positions).

2. Undulated lamina may cause a reduction of in-plane stiffness, and increased stress concentrations both at the lamina interfaces and in the nearby fiber-reinforced region located in the most curved regions. On one hand, the surface-lamina undulations are already being included partly in the out-of-plane undulation z_{out}. On the other hand, the inner-lamina

undulations are not included, but may be assumed to have an effect smaller than the surface undulations.

3. The minor geometrical distortions are smaller compared to the distortions caused by the structural yarn. Therefore, their effect is assumed negligible compared the distortions caused by the stitching yarn, as similar to the assumptions made in [42, 43].

6.3. On the use of the percentile for damage initiation indicators in linear elastic simulations

Linear elastic simulations have been used to capture the stiffness and the stress distribution changes that are caused by stitching. The stiffness has been computed using computational homogenisation principles (as has been outlined in [50]). The stress concentrations have been assessed using damage initiation indicators, for which a percentile value has been considered. The usefulness for a percentile on the damage initiation indicators to assess the stress concentrations caused by stitching is emphasised in the following:

1. Weak or strong stress concentrations will be present in the complex-shaped geometries of the stitched laminates. These stress concentrations are difficult to capture in linear elastic simulations, (1) for which strong mesh refinements are needed, and (2) are even impossible to capture if a singularity is present. By taking a percentile on the damage indicators, one attempts to look at regions in which the stress concentrations are above a certain level, so as to not look at the maximum value of the concentration itself, but rather to assess which regions are close to damage initiation. It allows the use of linear elastic simulations, while giving meaningful insights on the effect of stitching on stress concentrations.

2. The effect of stitching on the stiffness and on the potential for damage initiation is assessed by comparing stitched unit-cell models with a reference unstitched laminate. It is clear (from the results presented in Section 5) that stitching is causing increases in the damage initiation indicators near the stitch locations. These stress concentrations can be well presented using the percentile on the damage indicators. The information about these effects of the stitching on the damage indicators can be used, for example, to provide the right damage laws at the right locations in future simulations.

7. Conclusion

An approach was presented for the generation of mesoscopic unit-cell models for stitched non-crimp fabric composites. The shape of resin-rich regions, out-of-plane undulations and stitching yarn corresponding to different stitching yarn parameters could be obtained automatically by changing the parameters of geometrical operations. A fiber-reinforced distorted zone model could account for local changes in fiber-volume fraction and fiber directions in the fiber-reinforcement region. The importance of including the stitching yarn, out-of-plane undulations and local fiber-reinforcement distortions in models for stiffness and damage initiation prediction have been shown by mechanical simulations. While the main objective of the present work relied on presenting the novel RVE generation framework itself, an in-depth experimental program is part of future work.

Future work consists in: (1) performing an in-depth experimental study in which physical samples for different stitch parameters are generated, and geometrically and mechanically characterised to validate the approach, (2) extending the finite element models with more elaborated damage initiation models towards strength model predictions, and (3) using the framework to generate more realistic unit-cell models for different stitch parameters including undulated lamina, other stitch patterns, etc..

Acknowledgements

The first author acknowledges the support of IWT under Grant No. IWT-SB-678.

8. References

[1] K. Dransfield, C. Baillie, Y. Mai, Improving the delamination resistance of cfrp by stitching—a review, Composites Science and Technology 50 (3) (1994) 305–317.

[2] D. Shu, Y. Mai, Delamination buckling with bridging, Composites science and technology 47 (1) (1993) 25–33.

[3] H. Heß, N. Himmel, Structurally stitched ncf cfrp laminates. part 1: Experimental characterization of in-plane and out-of-plane properties, Composites Science and Technology 71 (5) (2011) 549–568.

[4] R. Velmurugan, S. Solaimurugan, Improvements in mode i interlaminar fracture toughness and in-plane mechanical properties of stitched glass/polyester composites, Composites Science and Technology 67 (1) (2007) 61–69.

[5] K. Tan, N. Watanabe, Y. Iwahori, T. Ishikawa, Effect of stitch density and stitch thread thickness on compression after impact strength and response of stitched composites, Composites Science and Technology 72 (5) (2012) 587–598.

[6] M. Wood, X. Sun, L. Tong, A. Katzos, A. Rispler, Y. Mai, The effect of stitch distribution on mode i delamination toughness of stitched laminated composites–experimental results and fea simulation, Composites Science and Technology 67 (6) (2007) 1058–1072.

[7] E. Wu, J. Wang, Behavior of stitched laminates under in-plane tensile and transverse impact loading, Journal of Composite Materials 29 (17) (1995) 2254–2279.

[8] A. Mouritz, K. Leong, I. Herszberg, A review of the effect of stitching on the in-plane mechanical properties of fibre-reinforced polymer composites, Composites Part A: applied science and manufacturing 28 (12) (1997) 979–991.

[9] A. Yudhanto, G. Lubineau, I. Ventura, N. Watanabe, Y. Iwahori, H. Hoshi, Damage characteristics in 3d stitched composites with various stitch parameters under in-plane tension, Composites Part A: Applied Science and Manufacturing 71 (2015) 17–31.

[10] V. Koissin, J. Kustermans, S. Lomov, I. Verpoest, B. Van Den Broucke, V. Witzel, Structurally stitched ncf preforms: quasi-static response, Composites science and technology 69 (15) (2009) 2701–2710.

[11] A. Mouritz, B. Cox, A mechanistic interpretation of the comparative in-plane mechanical properties of 3d woven, stitched and pinned composites, Composites Part A: Applied Science and Manufacturing 41 (6) (2010) 709–728.

[12] L. Asp, F. Edgren, A. Sjögren, Effects of stitch pattern on the mechanical properties of non-crimp fabric composites, Proceeding of the 11 ECCM (2004) 31–05.

[13] K. Vallons, G. Adolphs, P. Lucas, S. Lomov, I. Verpoest, The influence of the stitching pattern on the internal geometry, quasi-static and fatigue mechanical properties of glass fibre non-crimp fabric composites, Composites Part A: Applied Science and Manufacturing 56 (2014) 272–279.

[14] F. Edgren, C. Soutis, L. Asp, Damage tolerance analysis of ncf composite sandwich panels, Composites Science and Technology 68 (13) (2008) 2635–2645.

[15] T. Truong, M. Vettori, S. Lomov, I. Verpoest, Carbon composites based on multi-axial multiply stitched preforms. part 4. mechanical properties of composites and damage observation, Composites Part A: applied science and manufacturing 36 (9) (2005) 1207–1221.

[16] D. Mikhaluk, T. Truong, A. Borovkov, S. Lomov, I. Verpoest, Experimental observations and finite element modelling of damage initiation and evolution in carbon/epoxy non-crimp fabric composites, Engineering Fracture Mechanics 75 (9) (2008) 2751–2766.

[17] A. Yudhanto, N. Watanabe, Y. Iwahori, H. Hoshi, Effect of stitch density on tensile properties and damage mechanisms of stitched carbon/epoxy composites, Composites Part B: Engineering 46 (2013) 151–165.

[18] Y. Aono, K. Hirota, S. Lee, T. Kuroiwa, K. Takita, Fatigue damage of gfrp laminates consisting of stitched unit layers, International Journal of Fatigue 30 (10-11) (2008) 1720–1728.

[19] S. Lomov, D. Ivanov, I. Verpoest, M. Zako, T. Kurashiki, H. Nakai, S. Hirosawa, Meso-fe modelling of textile composites: Road map, data flow and algorithms, Composites Science and Technology 67 (9) (2007) 1870–1891.

[20] B. Piezel, B. Mercatoris, W. Trabelsi, L. Laiarinandrasana, A. Thionnet, T. J. Massart, Bending effect on the risk for delamination at the reinforcement/matrix interface of 3d woven fabric composite using a shell-like rve, Composite structures 94 (8) (2012) 2343–2357.

[21] A. Mouritz, B. Cox, A mechanistic approach to the properties of stitched laminates, Composites part A: applied science and manufacturing 31 (1) (2000) 1–27.

[22] D. Mattsson, R. Joffe, J. Varna, Methodology for characterization of internal structure parameters governing performance in ncf composites, Composites Part B: Engineering 38 (1) (2007) 44–57.

[23] S. Lomov, E. Belov, T. Bischoff, S. Ghosh, T. Chi, I. Verpoest, Carbon composites based on multiaxial multiply stitched preforms. part 1. geometry of the preform, Composites Part A: Applied science and manufacturing 33 (9) (2002) 1171–1183.

[24] G. Farley, L. Dickinson, Removal of surface loop from stitched composites can improve compression and compression-after-impact strengths, Journal of reinforced plastics and composites 11 (6) (1992) 633–642.

[25] Y. Wei, J. Zhang, Characterization of microstructure in stitched unidirectional composite laminates, Composites Part A: Applied Science and Manufacturing 39 (5) (2008) 815–824.

[26] R. Joffe, D. Mattsson, J. Modniks, J. Varna, Compressive failure analysis of non-crimp fabric composites with large out-of-plane misalignment of fiber bundles, Composites Part A: applied science and manufacturing 36 (8) (2005) 1030–1046.

[27] S. Drapier, M. Wisnom, A finite-element investigation of the interlaminar shear behaviour of non-crimp-fabric-based composites, Composites Science and Technology 59 (16) (1999) 2351–2362.

[28] S. Drapier, M. Wisnom, Finite-element investigation of the compressive strength of non-crimp-fabric-based composites, Composites Science and Technology 59 (8) (1999) 1287–1297.

[29] F. Edgren, L. Asp, Approximate analytical constitutive model for non-crimp fabric composites, Composites Part A: Applied Science and Manufacturing 36 (2) (2005) 173–181.

[30] D. Mattsson, R. Joffe, J. Varna, Damage in ncf composites under tension: effect of layer stacking sequence, Engineering Fracture Mechanics 75 (9) (2008) 2666–2682.

[31] R. Loendersloot, S. Lomov, R. Akkerman, I. Verpoest, Carbon composites based on multiaxial multiply stitched preforms. part v: geometry of sheared biaxial fabrics, Composites Part A: Applied Science and Manufacturing 37 (1) (2006) 103–113.

[32] G. Farley, A mechanism responsible for reducing compression strength of through-the-thickness reinforced composite material, Journal of composite materials 26 (12) (1992) 1784–1795.

[33] M. Nordlund, T. Lundstrom, Numerical study of the local permeability of noncrimp fabrics, Journal of composite materials 39 (10) (2005) 929–947.

[34] H. Heß, Y. Roth, N. Himmel, Elastic constants estimation of stitched ncf cfrp laminates based on a finite element unit-cell model, Composites Science and Technology 67 (6) (2007) 1081–1095.

[35] H. Heß, N. Himmel, Structurally stitched ncf cfrp laminates. part 2: Finite element unit cell based prediction of in-plane strength, Composites Science and Technology 71 (5) (2011) 569–585.

[36] T. Kurashiki, N. Watanabe, M. Matsushima, M. Zako, S. Lomov, I. Verpoest, Effects of stitching parameters on damage development for non-crimp fabric composites under tensile loading, in: 15th European Conference on Composite Materials (ECCM-15), 2012.

[37] T. Kurashiki, K. Hamada, S. Honda, M. Zako, S. Lomov, I. Verpoest, Mechanical behaviors of non-crimp fabric composites based on multi-scale analysis, in: 17th Int. Conf. on Composite Materials, Edinburgh, UK, 2009.

[38] A. González, E. Graciani, F. París, Prediction of in-plane stiffness properties of non-crimp fabric laminates by means of 3d finite element analysis, Composites Science and Technology 68 (1) (2008) 121–131.

[39] L. Ferreira, E. Graciani, F. París, Modelling the waviness of the fibres in non-crimp fabric composites using 3d finite element models with straight tows, Composite Structures 107 (2014) 79–87.

[40] L. Ferreira, E. Graciani, F. París, Three dimensional finite element study of the behaviour and failure mechanism of non-crimp fabric composites under in-plane compression, Composite Structures 149 (2016) 106–113.

[41] J. Netz, B. Hannemann, S. Schmeer, Micro-leveled modeling of structural stitched frp joints as energy absorbing rupture points, Composite Structures 157 (2016) 131–140.

[42] G. Pierreux, L. Wu, D. Van Hemelrijck, T. J. Massart, Evaluation of microdamage initiation in z-pinned laminates by means of automated rve computations, Composite Structures 206 (2018) 104–115.

[43] G. Pierreux, D. Van Hemelrijck, T. J. Massart, Automated generation of 3d orthogonal woven composites rves including yarn cross-section variations, Composites science and technology 176 (2019) 90–102.

[44] G. Zhou, X. Sun, Y. Wang, Multi-chain digital element analysis in textile mechanics, Composites science and Technology 64 (2) (2004) 239–244.

[45] L. Daelemans, J. Faes, S. Allaoui, G. Hivet, M. Dierick, L. Van Hoorebeke, W. Van Paepegem, Finite element simulation of the woven geometry and mechanical behaviour of a 3d woven dry fabric under tensile and shear loading using the digital element method, Composites Science and Technology 137 (2016) 177–187.

[46] S. Green, M. Matveev, A. Long, D. Ivanov, S. Hallett, Mechanical modelling of 3d woven composites considering realistic unit cell geometry, Composite Structures 118 (2014) 284–293.

[47] A. Thompson, B. El Said, D. Ivanov, J. Belnoue, S. Hallett, High fidelity modelling of the compression behaviour of 2d woven fabrics, International Journal of Solids and Structures.

[48] B. El Said, S. Green, S. Hallett, Kinematic modelling of 3d woven fabric deformation for structural scale features, Composites Part A: Applied Science and Manufacturing 57 (2014) 95–107.

[49] D. Durville, Simulation of the mechanical behaviour of woven fabrics at the scale of fibers, International journal of material forming 3 (2) (2010) 1241–1251.

[50] G. Pierreux, Automated unit-cell model generation for micro-mechanical simulations of 3d reinforced composites, Ph.D. thesis, Université libre de Bruxelles and Vrije Universiteit Brussel, Brussels (2018).

[51] B. Sonon, B. Francois, T. J. Massart, A unified level set based methodology for fast generation of complex microstructural multi-phase rves, Computer methods in applied mechanics and engineering 223 (2012) 103–122.

[52] B. Wintiba, B. Sonon, K. Kamel, T. J. Massart, An automated procedure for the generation and conformal discretization of 3d woven composites rves, Composite Structures 180 (2017) 955–971.

[53] S. Lomov, G. Huysmans, Y. Luo, R. Parnas, A. Prodromou, I. Verpoest, F. Phelan, Textile composites: modelling strategies, Composites Part A: applied science and manufacturing 32 (10) (2001) 1379–1394.

[54] C. Chamis, Mechanics of composite materials: past, present, and future, Journal of Composites, Technology and Research 11 (1) (1989) 3–14.

[55] B. Rosen, Tensile failure of fibrous composites, AIAA journal 2 (11) (1964) 1985–1991.

[56] A. Kaddour, M. Hinton, P. Smith, S. Li, Mechanical properties and details of composite laminates for the test cases used in the third world-wide failure exercise, Journal of Composite Materials 47 (20-21) (2013) 2427–2442.

[57] A. Turon, P. P. Camanho, J. Costa, C. Dávila, A damage model for the simulation of delamination in advanced composites under variable-mode loading, Mechanics of Materials 38 (11) (2006) 1072–1089.

[58] A. Bogdanovich, M. Karahan, S. Lomov, I. Verpoest, Quasi-static tensile behavior and damage of carbon/epoxy composite reinforced with 3d non-crimp orthogonal woven fabric, Mechanics of Materials 62 (2013) 14–31.

[59] D. Ivanov, S. Lomov, A. Bogdanovich, M. Karahan, I. Verpoest, A comparative study of tensile properties of non-crimp 3d orthogonal weave and multi-layer plain weave e-glass composites. part 2: Comprehensive experimental results, Composites part a: applied science and manufacturing 40 (8) (2009) 1144–1157.

[60] A. Puck, H. Schürmann, Failure analysis of frp laminates by means of physically based phenomenological models, in: Failure Criteria in Fibre-Reinforced-Polymer Composites, Elsevier, 2004, pp. 832–876.

[61] Z. Hashin, Failure criteria for unidirectional fiber composites, Journal of applied mechanics 47 (2) (1980) 329–334.

[62] Y. Mahadik, S. Hallett, Finite element modelling of tow geometry in 3d woven fabrics, Composites Part A: Applied Science and Manufacturing 41 (9) (2010) 1192–1200.